Correspondence to:
X. Wang,
xgwang@pku.edu.cn

Reconstruction of Local Magnetic Structures by a Modified Radial Basis Function Method

Wenming Chen[1] [iD], **Xiaogang Wang[2]**, **N. A. Tsyganenko[3]** [iD], **V. A. Andreeva[3]** [iD], and **V. S. Semenov[3]** [iD]

[1]School of Physics, Fusion Simulation Center, State Key Lab of Nuclear Physics & Technology, Peking University, Beijing, China, [2]Department of Physics, Harbin Institute of Technology, Harbin, China, [3]Department of Geophysics, St. Petersburg State University, St. Petersburg, Russia

Abstract Local magnetic structures in space environments, in particular, those in the diffusion region such as magnetic nulls or separators, are very difficult to identify by satellite measurements but important for understanding of magnetic reconnection. Multi-spacecraft missions such as Cluster or MMS, however, provide an opportunity to reconstruct the fine structures using vector data of space magnetometers. In this paper, we introduce a method for such a local reconstruction, based on the modified radial basis functions (Andreeva & Tsyganenko, 2016, https://doi.org/10.1002/2016JA023217), used previously for the global magnetic field modeling. A principal advantage of this method is its freedom from a priori assumptions on the magnetic field topology. The method has been tested on $2\frac{1}{2}$ and 3D reconnection geometries and provided a good agreement with preset models. The relative errors of null positions, γ-line directions, and $\sum$-surface normal directions are found to be below 6% even with 20% random errors added to the target magnetic field vectors in reconstruction of 3D separator model geometry. Applications of the method to the field reconstruction based on Cluster measurements are also presented and discussed.

1. Introduction

Mapping and data-based reconstruction of various magnetic structures in space, such as those associated with flux ropes or ion/electron diffusion regions around the reconnection sites, are the first step toward better understanding of their formation and evolution. Methods have been proposed to develop an empirical description of the global geomagnetic field, strongly affected by space weather events and revealing highly complex geometry and structure (Tsyganenko, 1995, 2014). Methods to recover coherent magnetic structures and magnetic flux ropes have also been developed by assuming a 2D (Hau & Sonnerup, 1999; Hu & Sonnerup, 2001) or 3D (Hasegawa et al., 2015) stationary state in a co-moving frame of reference. Recently, it is extended to reconstruction of electron diffusion region based on electron magnetohydrodynamic equations while it assumes a 2D stationary state (Hasegawa et al., 2019). Fine local structures in 3D space, such as nulls or separators which are possible sites for reconnection, have also been reconstructed based on a static Harris current sheet model (He et al., 2008). However, magnetic reconnection, a key phenomenon in a wide variety of astrophysical processes, is in general a highly dynamical non-stationary process (Øieroset et al., 2001; Parker, 1957; Yamada et al., 2010), which implies that the Harris current sheet model may be hardly applicable.

In this paper, we describe results of applying another reconstruction approach, the radial basis function (RBF) method, originally proposed by Andreeva and Tsyganenko (2016) and Tsyganenko and Andreeva (2016). Its essence is to represent the global magnetospheric magnetic field by formally expanding it into a flexible series of terms, without any pre-conceived assumptions or restrictions on the structure of principal field sources. Here we further develop that method, previously used in the global modeling, to reconstruct local field structures associated with reconnection geometries in 3D space, using time series of spacecraft data.

The simplest method to identify a magnetic null from multi-point satellite measurements is to compute the Poincare index (Greene, 1992; Xiao et al., 2006). However, that approach is very sensitive to the magnitude of fluctuations, which can produce misleading results. Also, due to the complex configuration of three-dimensional (3D) reconnection (Lau & Finn, 1990; Pontin, 2011; Priest & Titov, 1996), the satellite data cannot directly describe the 3D geometry of the magnetic field and the plasma flow patterns. By expanding the

magnetic field into a weighted sum of modified RBFs (M-RBF), all restrictions on the magnetic field structure can be removed from the outset.

The paper is organized as follows. Section 2 systematically describes specific details of the method. Section 3 presents results of testing the method on a 2D reconnection geometry, where the satellite trajectory and guide field direction form an angle less than 10 degrees, and on a 3D reconnection geometry which comprises two different types of nulls with a current flowing along the separator line (Pontin, 2011; Xiao et al., 2007). In section 4, we apply the method to an observed reconnection event, already well-studied by others, to show that the method can resolve the intrinsic current system. The paper is concluded by a summary and a brief discussion in section 5.

2. Method Description

We focus on short time periods when the varying magnetic structure can be assumed static, which allows us to reconstruct it by formally decomposing the field into a weighted sum of radial basis functions and then fit the model to spacecraft data. Due to the divergenceless nature of the magnetic field, it is convenient to represent the field as a sum of toroidal and poloidal components (e.g., Stern, 1976, and references therein):

$$\overrightarrow{B} = \nabla\times\left(\frac{\psi_1}{r}\overrightarrow{r}\right) + \nabla\times\nabla\times(\psi_2\overrightarrow{r}) \tag{1}$$

The next step is to decompose the toroidal and poloidal potentials ψ_1 and ψ_2, into linear combinations of modified radial basis functions (Andreeva & Tsyganenko, 2016; Tsyganenko & Andreeva, 2016)

$$\psi = \sum_i \alpha_i \chi_i \tag{2}$$

$$\chi_i\left(\overrightarrow{r}; D, \overrightarrow{L}\right) = \sqrt{\left(\frac{x-R_{i,x}}{L_x}\right)^2 + \left(\frac{y-R_{i,y}}{L_y}\right)^2 + \left(\frac{z-R_{i,z}}{L_z}\right)^2 + D^2} \tag{3}$$

where the vectors $\overrightarrow{R}_i$ are coordinates of meshwork grid nodes and D is an adjustable regularization parameter. The advantage of this approach is the number of nodes, that is, the resolution of the reconstructed field can be adjusted in different situations. Note that the scale length that measurements can resolve in the direction perpendicular to the space probe trajectories is limited by the separation of the probes, which is much larger in comparison with the spatial separation of consecutive data sampling along the spacecraft orbits. If there is short wavelength variation along the orbits, whose length scale is comparable with the spatial separation of consecutive measurements, the reconstructed field based on the original isotropic RBF expansions will contain artificial variation in the perpendicular direction which cannot be resolved by the constellation of satellites. To avoid them, we introduce in this work a modification to the original method, which is to separately scale the distances entering in RBFs by characteristic lengths $\{L_x, L_y, L_z\}$, equal to the node separation along each axis. This makes it possible to resolve short scale lengths along the probe trajectories and, at the same time, avoid artificial unphysical fluctuations on the perpendicular surface.

Figure 1 illustrates a simple example of the node meshwork, where we attach the reference frame to the moving bulk plasma (and, hence, to the frozen-in magnetic structure), so that it is the satellites that move through the magnetic structure. Thus, the measurements at various moments can be taken at various points with the distance between two points given by the structure moving velocity multiplied by the time interval between the measurements. Red diamonds in Figure 1 represent the positions where the measurements are taken, and the node positions are shown by green circles located on the boundary. For simplicity, we place the four probes on the same plane for every measurement time moment and define that plane as the probe moving surface. Without loss of generality, we define the moving direction as *y*-axis. Because the dependence of the reconstructed field on *y* can be resolved by different nodes along *y*-axis, the dependence of the reconstructed field on the other two coordinates must be resolved by different nodes on the same probe moving surface. On that surface, the probe's projections can always form a rectangle whose edges are parallel to *x*- or *z*-axis with the projections located on or enclosed by the edges. In order to obtain a decent coverage of the reconstruction domain, we expand the rectangle by a factor 1.4 (the ratio of length of edges before and after the expanding) by fixing its geometry center and place four nodes on the vertices of that rectangle, so
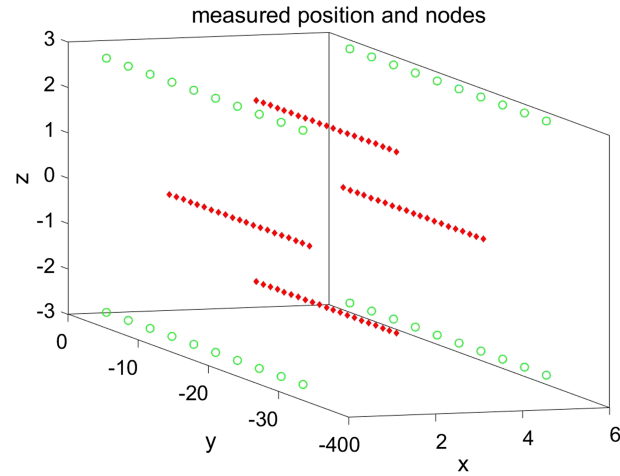
Figure 1. Illustration of probe positions (red diamonds) and nodes (green circles).

that parameters on each node can be influenced by two nearest measurements. The final picture can be summarized by 0. We must note that more than four nodes on one probe moving surface will increase the degeneracy of the reconstruction because of four measurements at one time moment. There are several other ways to place the nodes, but the method described above turns out to be simple and efficient.

The essence of the reconstruction task is to determine the expansion coefficients $\{\alpha_i\}$ from the data. By substituting equation (3) into equation (3) and then equation (1), one could obtain explicit equations for the magnetic field components. When arranging all the magnetic field components at all measurement positions into one vector, one can formulate the inverse problem in a matrix form. For instance, at the mth measurement location, the contribution from the nth node will read:

$$
\begin{pmatrix} \vdots \\ B_{xm} \\ B_{ym} \\ B_{zm} \\ \vdots \end{pmatrix} = \begin{pmatrix} \ddots & & \vdots & & \iddots \\ & A_{xm}^{1n} & A_{xm}^{2n} & \\ \cdots & A_{ym}^{1n} & A_{ym}^{2n} & \cdots \\ & A_{zm}^{1n} & A_{zm}^{2n} & \\ \iddots & & \vdots & & \ddots \end{pmatrix} \cdot \begin{pmatrix} \vdots \\ \alpha_{n1} \\ \alpha_{n2} \\ \vdots \end{pmatrix}
\tag{4}
$$

where

$$
\begin{pmatrix} A_{xm}^{1n} \\ A_{ym}^{1n} \\ A_{zm}^{1n} \end{pmatrix} = \frac{1}{r} \begin{pmatrix} z\dfrac{\partial}{\partial y} - y\dfrac{\partial}{\partial z} \\ x\dfrac{\partial}{\partial z} - z\dfrac{\partial}{\partial x} \\ y\dfrac{\partial}{\partial x} - x\dfrac{\partial}{\partial y} \end{pmatrix} \chi_{mn}
$$

$$
\begin{pmatrix} A_{xm}^{2n} \\ A_{ym}^{2n} \\ A_{zm}^{2n} \end{pmatrix} = \begin{pmatrix} 2\dfrac{\partial}{\partial x} + \left(x\dfrac{\partial^2}{\partial x \partial x} + y\dfrac{\partial^2}{\partial y \partial x} + z\dfrac{\partial^2}{\partial z \partial x} \right) - x\nabla^2 \\ 2\dfrac{\partial}{\partial y} + \left(x\dfrac{\partial^2}{\partial x \partial y} + y\dfrac{\partial^2}{\partial y \partial y} + z\dfrac{\partial^2}{\partial z \partial y} \right) - y\nabla^2 \\ 2\dfrac{\partial}{\partial z} + \left(x\dfrac{\partial^2}{\partial x \partial z} + y\dfrac{\partial^2}{\partial y \partial z} + z\dfrac{\partial^2}{\partial z \partial z} \right) - z\nabla^2 \end{pmatrix} \chi_{mn}
$$

that is, $\boldsymbol{B} = \widehat{\mathbf{A}} \boldsymbol{\alpha}$. Here $\boldsymbol{B}$ is a $3M$-dimensional vector composed of M measured field vectors with three components at each location, and $\boldsymbol{\alpha}$ is a $2N$-dimensional coefficient vector, corresponding to $N(<M)$ nodes, with two radial basis functions for each node. The matrix $\widehat{\mathbf{A}}$ contains $3M \times 2N$ elements derived from equations (1) and (3). The problem is now reduced to the derivation of the coefficients $\boldsymbol{\alpha}$ from equation (4) by inverting the

equation $\boldsymbol{B} = \widehat{\mathbf{A}}\boldsymbol{\alpha}$ and thus reconstructing the magnetic field distribution in the 3D domain of interest. We assume the number of observations to be greater than the number of deposited nodes, for which reason the matrix $\widehat{\mathbf{A}}$ is not square and, hence, not directly invertible. To solve the inverse problem, we apply singular value decomposition (Golub, 1970) to the matrix $\widehat{\mathbf{A}}$ and find its pseudoinverse, which makes it possible to construct an optimal solution. Specifically, let us decompose $\widehat{\mathbf{A}}$ as $\widehat{\mathbf{V}}\widehat{\textstyle\sum}\widehat{\mathbf{U}}^{\mathrm{T}}$, where the matrix $\widehat{\textstyle\sum}$ contains l ($l \leq \min(3M, 2N)$) nonzero singular values $\{s_i\}$, $\widehat{\mathbf{V}}$ contains corresponding normalized orthogonal magnetic field value vectors $\{\boldsymbol{v}_i\}$, and $\widehat{\mathbf{U}}$ contains normalized orthogonal coefficient vectors $\{\boldsymbol{u}_i\}$. Then the desired optimal solution is

$$\boldsymbol{\alpha} = \sum_{i=1}^{l} \boldsymbol{u}_i s_i^{-1}\left(\boldsymbol{v}_i^T \cdot \boldsymbol{B}\right) \tag{5}$$

The Euclidean norm of $\boldsymbol{\alpha}$ becomes large if the right-hand side of equation (5) contains very small singular values, resulting in large spatial fluctuations of the reconstructed field, as illustrated in the 1D case shown in the left plot of Figure 2. By discarding very small singular values, we can avoid such fluctuations in the modeling domain.

To determine the model's free parameter D, we performed tests using, for simplicity, a 1D model. The sample configuration is a Harris current sheet where the magnetic field varies across the sheet as $y = \mathrm{tahn}(x)$ with measurements randomly distributed over $M = 20$ positions within the interval $x \in (-6, 6)$, to imitate the measurements taken by a single satellite moving across the sheet. Then we uniformly place $N = 20$ nodes in the sampling interval and reconstruct the model function using the measured values and corresponding positions as input.

Since the modeled function is a scalar, we directly represent it as a summation of basis functions $y' = \sum_{i=1}^{i=N}$ $\chi_{\overrightarrow{R}_i}(x)$, where $\chi_{\overrightarrow{R}_i}(x) = \sqrt{\left(\dfrac{x - R_x}{L_x}\right)^2 + D^2}$. The results are shown in Figure 2, where L_x is set equal to unity.

The red stars are measured values at randomly distributed measurement positions, the blue circles represent the reconstructed values at node positions, and the solid curve is the reconstructed magnetic field. The left plot is the result with D equal to the node separation, which demonstrates that even though local values of the reconstructed field are the same as those of the model field at measurement positions, the reconstructed curve dramatically deviates from the model field. The right plot shows the result of setting D three times of the node separation. In this case, by contrast, the reconstructed function fits the target function much better. In other words, in the 3D case, when $\{L_x, L_y, L_z\}$ is set equal to the node separation along each axis, setting D to be three would lead to optimal results.

3. Reconstruction of Model Magnetic Field

To test the proposed method, we apply it to 2D reconnection geometry with a guide field, because the 2D case has been widely studied in theory and simulation (Birn et al., 2001; Pritchett, 2004) and certain features such as Hall quadruple components have been identified in satellite observations (Eastwood et al., 2007). Distributing vectors continuously along a specific direction, say in y-direction, we can treat them as spacecraft magnetic field data. First, we set a simple X-point reconnection model, composed of an equilibrium magnetic field described by flux function $\psi_0(x)$ corresponding to a Harris current sheet flowing along the z-direction, and with a y-directed guide field. Magnetic island is represented by the flux function $\widetilde{\psi} = \delta\cos$ $(k_x x)\cos(k_z z)$. Then the total model magnetic field $\overrightarrow{B} = \nabla\psi \times \widehat{e}_y + B_y \widehat{e}_y$, and

$$B_z = \frac{\partial}{\partial x}\psi_0 + \frac{\partial}{\partial x}\widetilde{\psi} = \tanh\frac{x}{L} - k_x \delta\sin(k_x x)\cos(k_z z) \quad B_x = -\frac{\partial}{\partial z}\widetilde{\psi} = k_z \delta\cos(k_x x)\sin(k_z z).$$

All variables here are dimensionless, with the magnetic field normalized by $B_0 = 1$ nT, and the length by $L_0 = 100$ km.

In order to model a general magnetic field encountered by satellites in space, we rotate the above magnetic structure around the y-axis by an angle θ_y first, and then by an angle θ_z around the new z-axis. Without loss
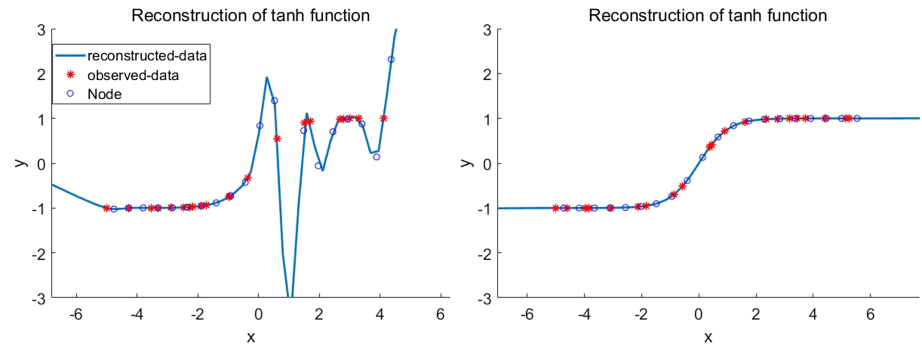
Figure 2. The sample test of 1D reconstruction. Left: the parameter $|D|$ is equal to the node separation; right: D is three times the separation.

of generality, we further set the moving direction of satellites along the new y-axis. By changing the angle parameters, we can cover almost all situations encountered by satellites in real space.

Figure 3 shows a case of $L = 3, k_x = \frac{2\pi}{6L}, k_z = \frac{2\pi}{3L}, \delta = 0.5, B_y = 0.5,$ and $\theta_z = 10°, \theta_y = 45°$, where diamonds are virtual satellite probes, circles are the nodes, streamlines represent field lines, and contour lines show the magnitude of error field which is defined by $\left| \overrightarrow{B}_{rec} - \overrightarrow{B}_{model} \right|$. Separation of nearby probes is 2 in both x- and z-directions, with the in-plane distance between the leftmost and the rightmost probes being equal to 4. In addition, the distance between two adjacent probe moving surfaces is unity along the y-direction. We then take 21 measurements for each satellite, ranging in $y \in [-27, -7]$. The configuration of the preset model magnetic field is shown in the left column of Figure 3. The upper plot is at the moment as the rightmost satellite encounters the X-point, the middle one shows the next moment, and the bottom plot is for the moment
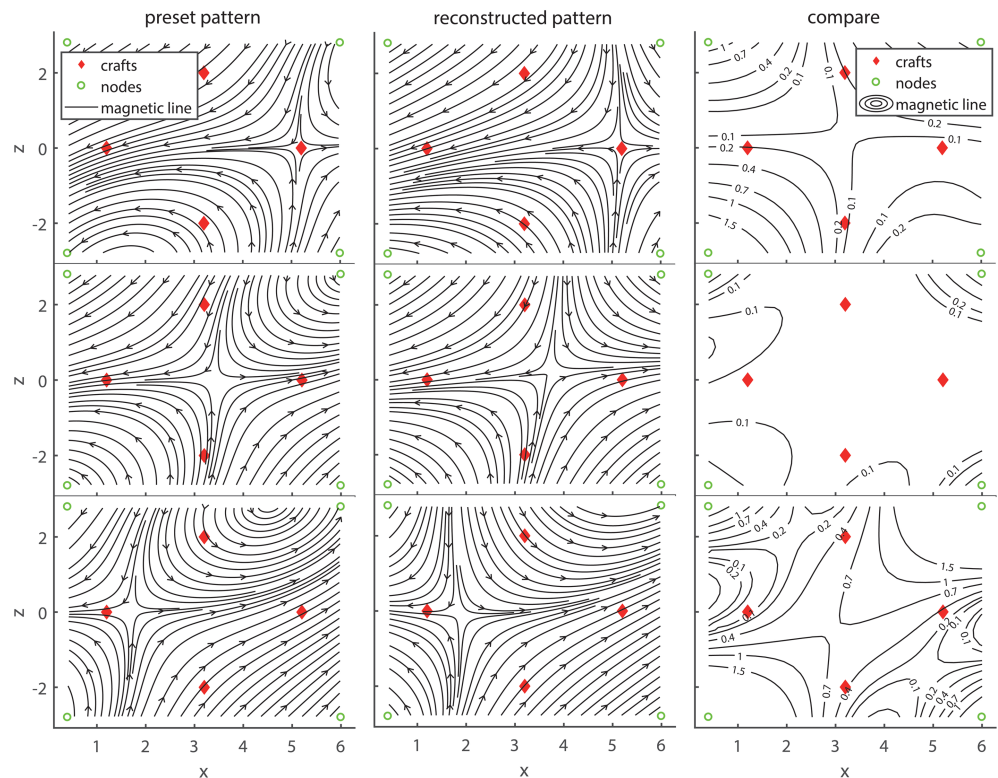

Figure 3. 2D X-point geometry with magnetic field being streamlined. Diamonds and circles represent the satellites and nodes, respectively. The left column is the preset model field, the middle is reconstructed results, and the right is their difference, showing snapshots for three consecutive time moments from top to bottom.
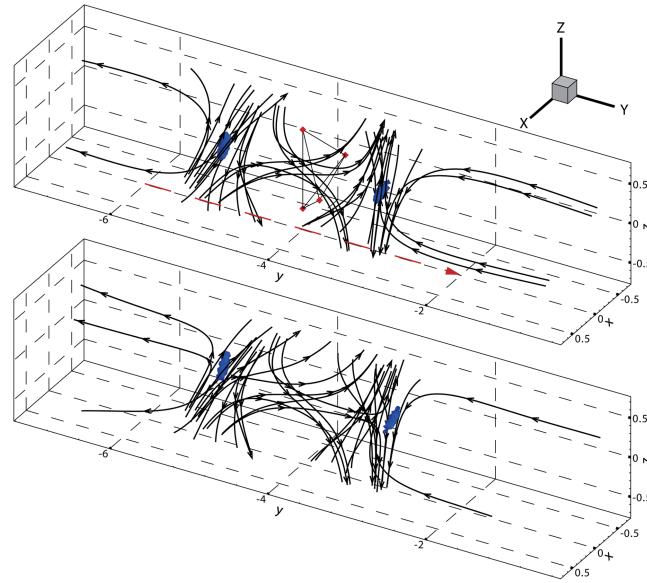
Figure 4. A separator model field (upper) with current and corresponding reconstructed field (lower). Arrowed streamlines are field lines. The red dotted arrowed line in the upper panel indicates the satellite moving direction. Red solid diamonds represent four satellites, forming a tetrahedron located at $(0, -4, -0.5)$, $(0.5, -3.5, 0)$, $(0, -4, 0.5)$, and $(-0.5, -3.75, 0)$, respectively, at the moment. In addition, iso-surface shows the magnetic field magnitude $\left|\overrightarrow{B}\right| = 0.15$.

when the leftmost craft encounters the X-point. The model field is assumed 2D and static during the measurement time interval, such that the three snapshots represent the x-z configuration of the magnetic field at three different y-positions at the same moment.

We evenly place 10 nodes along the y-direction with four nodes on each x-z plane, around the measurement region surrounded by measurement positions as shown in Figure 1. Shown in the middle column of Figure 3 is the reconstructed field and one can see a close agreement between the reconstructed and the preset model field in terms of magnetic field geometry. In the center of the measurement region shown by the middle plot of the right column in Figure 3, the magnitude of the error field is less than 0.1 nT compared with the magnitude of the modeled equilibrium field of ~1 nT. The error however becomes large at the boundary of the measurement region although this method successfully recovers the magnetic field geometry. Note that the spatial separation of the satellites should be less than the thickness of the current sheet in order for the measurements to resolve the magnetic structure. It can be a criterion for selecting data in real measurements.

The real magnetic field configurations are always 3D, which makes them hard to be reconstructed by single satellite data. Using multi-satellite data can be much more helpful to solving that problem. In particular, magnetic nulls and separatrices are of special interest as possible sites for the reconnection, so we focus our reconstruction on separators and nulls. A separator should comprise of two different polarity nulls, with one null's spine (or γ-line) locates on the other null's fan (or Σ-surface), and thus the separator is the intersection of two fans of the two nulls. Around a null positioned at $\overrightarrow{x}_0$, we can approximate magnetic field as $\boldsymbol{B}(\boldsymbol{x}) = \widehat{\boldsymbol{\delta B}} \cdot (\boldsymbol{x} - \boldsymbol{x_0})$, where $\widehat{\boldsymbol{\delta B}}$ is the gradient tensor at the null. In the matrix form, we can classify nulls according to the eigenvalue of $\widehat{\boldsymbol{\delta B}}$. We will call a null an A-type, if there is only one positive eigenvalue. The corresponding eigenvector is its γ-line, and the plane determined by the rest two eigenvectors is its Σ-surface. Such a null will be called A_s-type if the rest two eigenvalues are complex conjugates. Otherwise it is B-type or B_s-type. A separator reconnection geometry comprises a pair of $A(A_s)$- and $B(B_s)$-type nulls, whose configuration is analogous to the 2D X-point model as one views it along the separator. We adopt following separator model function (Pontin, 2011) with a current flowing along separator line represented by a factor of J_s, as

Table 1
Properties of the Model Nulls

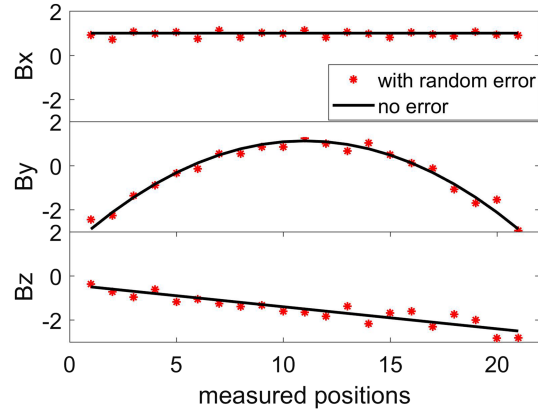| Type	Position	Eigenvalue	Eigenvector
B	$x = 0$	$\lambda_1 = -\sqrt{5} - 1$	$\overrightarrow{a}_1 = (-0.93,\ 0,\ 0.36)$
	$y = -5$	$\lambda_2 = 2$	$\overrightarrow{a}_2 = (0, 1,\ 0)$
	$z = 0$	$\lambda_3 = \sqrt{5} - 1$	$\overrightarrow{a}_3 = (0.36,\ 0,\ -0.93)$
A	$x = 0$	$\mu_1 = \sqrt{5} + 1$	$\overrightarrow{b}_1 = (0.36,\ 0,\ -0.93)$
	$y = -3$	$\mu_2 = -2$	$\overrightarrow{b}_2 = (0,\ 1,\ 0)$
	$z = 0$	$\mu_3 = -\sqrt{5} + 1$	$\overrightarrow{b}_3 = (-0.93,\ 0,\ 0.36)$

Figure 5. Magnetic field measured by the first craft. Black solid lines represent the preset model value, and red asterisks represent measured values with random errors.

$$
\begin{pmatrix} B_x \\ B_y \\ B_z \end{pmatrix} = B_0 \left(\begin{pmatrix} x(y'-3y_0) \\ y_0^2-y'^2+\frac{1}{2}(x^2+z^2) \\ z(y'+3y_0) \end{pmatrix} + J_s \begin{pmatrix} -\frac{1}{2}z\exp\left(-\frac{x^2+z^2}{2w^2}\right) \\ 0 \\ \frac{1}{2}x\exp\left(-\frac{x^2+z^2}{2w^2}\right) \end{pmatrix} \right), \quad y' = y-y_{\text{offset}}.
$$

The normalization used here is the same as in the 2D case, and additionally, the current is normalized by $\frac{1\ \text{nT}}{\mu_0 \times 100\ \text{km}} \approx 7.96\ \text{nA}$ according to Ampere's law.

Following is a typical case, as shown in the upper plot of Fiugre 4, featured by (1) the satellites moving along separator, (2) the average separation between them around unity, (3) the distance of 0.2 between adjacent probe moving surfaces, (4) the null separation of 2, and (5) the whole probe constellation traveling length of 4.

The upper plot in Figure 4 shows the magnetic configuration when $B_0 = 1$, $J_s = 4$, $y_0 = 1$, $y_{\text{offset}} = -4$, $w = 10$. One can clearly see the twisting magnetic lines around the separator line. On the left is a B-type with its γ-line parallel to the Σ-surface of the right null, and on the right is an A-type with its γ-line parallel to the left null's Σ-surface. Specific properties of the nulls are listed in Table 1.

To imitate a real measurement, we evenly randomly add errors to the measured values. Since the satellite measurement position relative to magnetic structure is fairly uncertain, we add up to a 50% relative error to the measurement positions, that is, one half the distance between adjacent probe moving surfaces along the moving direction and approximately a 20% relative error in other directions. For measured magnetic field values, the added error is up to 0.2 B_0, leading to a total of 10% relative error of the measured value compared with the model value shown in Figure 5, where red stars represent the measured values of the first craft and the solid line represents the corresponding no-error preset model values.

We place 40 nodes in total around the measurement positions, so that there are 80 parameters and 80 basic magnetic structures. Figure 6 shows, in this typical situation, the singular values (only the first 40 values are presented) and the amplitude of corresponding field value vectors $\{\nu_i\}$ contained in the measured value vector $\boldsymbol{B}$. To ensure the discrepancy between the reconstructed and measured fields at measurement positions remaining small, we ignore those basic magnetic structures with small amplitudes and very small singular values. Specifically, we retain 10 largest components, shown by the asterisks in the left plot of Figure 6, to reconstruct the 3D magnetic field, shown by the left plot of Figure 7. Noting that the singular value of the 27th basic magnetic structure in this measurement is much lower than the maximum, that is, $\frac{|s_{27}|}{s_{\max}} \ll 1$, one could discard it. However, since it makes a very large contribution to the measurement value vector due to the fact that the amplitude $|\mu_{27}|$ is the maximum shown in the left plot of Figure 6, we have to keep it for the reconstruction.
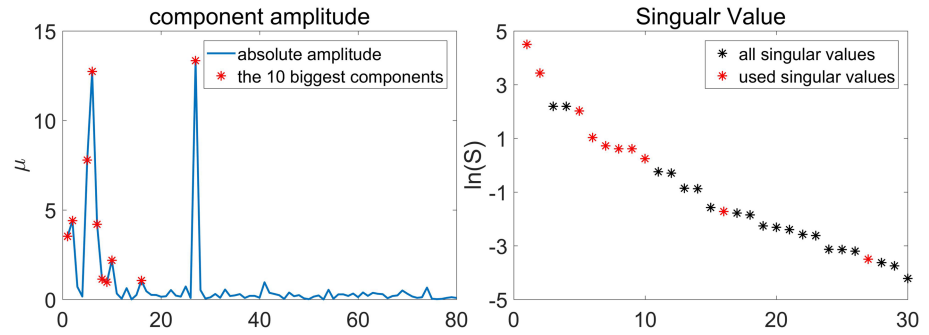
Figure 6. Component amplitudes (left) and singular values (right). Asterisks shown are 10 biggest components.

The reconstructed field is shown in the bottom plot of Figure 4, where the blue contour surface indicates an equal intensity surface surrounding a null for a magnetic magnitude $\left|\vec{B}\right| = 0.15$. The properties of reconstructed nulls are listed in Table 2. One can see that even though significant random errors have been added beforehand, the distance between the reconstructed and modeled nulls, that is, the relative error of null positions, is below 6% of the separator length; the angle between the reconstructed nulls' γ-lines and the model, that is, the relative error of the γ-line directions, is below 2% of 180 degrees; and the angle between the reconstructed Σ-surface's normal directions and the model, that is, the relative error of the Σ-surface normal directions, is below 1% of 180 degrees. Therefore, this reconstruction approach can reproduce the geometry of the structures quite well.

It is of interest to compare not only the magnetic topology but also the magnetic field intensity. The upper plot of Figure 7 shows the difference between reconstructed and measured magnetic fields at measurement positions of the first probe which shows a small deviance of the reconstructed field from the model. This is more explicit shown in the lower plot of Figure 7 where the blue contour shows the magnitude of an error vector field defined by $\left|\Delta\vec{B}\right| \equiv \left|\vec{B}_{\text{model}} - \vec{B}_{\text{rec}}\right| = 0.2$ nT, reasonably small in comparison with the measured field value, several nanotesla. And the red contour signifies the magnitude of $\left|\Delta\vec{B}\right| = 0.4$ nT surrounding the green contour surface, which means a smaller error in inner region. However, we must point out that the error may quickly increase outside the measurement region surrounded by measurement positions due to the lack of nonlocality of radial basis functions.
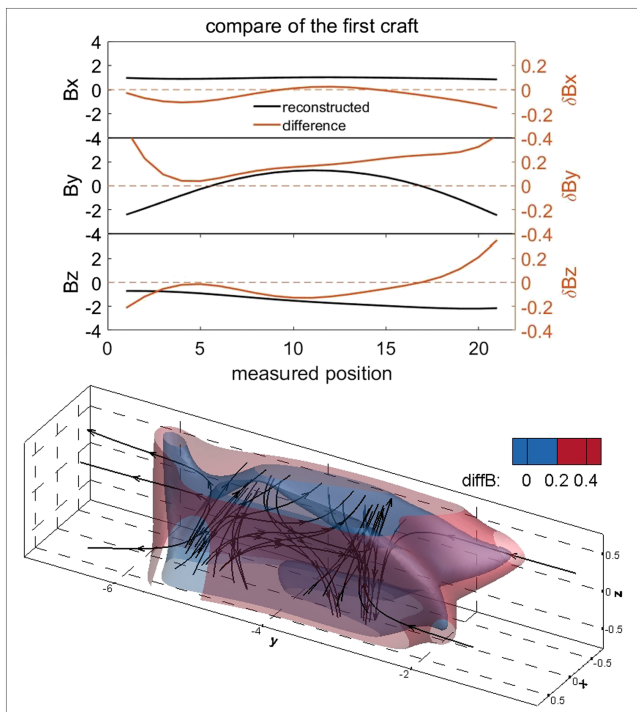
Note that the strength J_s and thickness w of the current sheet in Pontin's separator model is somewhat artificial. To test the method, we should apply it to several different cases with different strengths and thicknesses. When the current is strong enough, for example, $J_s > 6$, the model will comprise of a A_s and a B_s type null, but both with a y-directional γ-line which is not the case of real world. Because exploring that the separator model is beyond the scope of this paper, we focus the test on different thicknesses and found that the thicker current sheet is, the more accurate the reconstructed field is. This is a naturally expected result, because a thicker current sheet is easier to detect from satellite data against a noisy background.

Figure 7. Comparison of reconstructed and measured field value. The upper plot is for Craft-1, with red lines are difference between them and black lines represent the reconstructed field. The lower plot shows a blue contour of $\left|\Delta\vec{B}\right| = 0.2$ and a red contour of $\left|\Delta\vec{B}\right| = 0.4$ in the 3D domain interested.

4. Reconstruction Applied to Cluster Four-Spacecraft Measurements

We apply the method to reconstruct a real case of Cluster constellation wandering around a magnetic reconnection region in the magnetotail

Table 2
Properties of Reconstructed Nulls

Type	Position	Eigenvalue	Eigenvector	Norm of $\sum$-surface/γ-line
B	$x = -0.04$	$\lambda_1 = -3.29$	$\vec{a}_1 = (-0.93, 0.05, 0.35)$	$\hat{e}_\gamma = (-0.93, 0.05, 0.35)$
	$y = -5.01$	$\lambda_2 = 1.12$	$\vec{a}_2 = (-0.35, 0.02, 0.94)$	$\vec{n}_\Sigma = (0.93, 0.00, 0.35)$
	$z = 0.07$	$\lambda_3 = 2.17$	$\vec{a}_3 = (0.04, -0.99, -0.10)$	
A	$x = -0.07$	$\mu_1 = 3.34$	$\vec{b}_1 = (0.36, -0.01, -0.93)$	$\vec{e}_\gamma = (0.36, -0.01, -0.93)$
	$y = -2.93$	$\mu_2 = -1.15$	$\vec{b}_2 = (0.93, -0.04, -0.36)$	$\vec{n}_\Sigma = (0.35, 0.00, 0.93)$
	$z = 0.04$	$\mu_3 = -2.19$	$\vec{b}_3 = (0.12, 0.99, -0.05)$	

on 1 October 2001 between 09:36 UT and 09:55 UT, already studied extensively (e.g., Runov et al., 2003; Xiao et al., 2007). In particular, Guo et al. (2013) reconstructed the magnetic geometry by expanding the magnetic field into a sum of 10 spherical harmonic functions with an added Harris current sheet, a method first developed by He et al. (2008), and found a separator. Here we apply the M-RBF approach without any explicitly introduced current sheet to do reconstruction by utilizing a time series of Cluster data from 09:48:23 UT to 09:48:33 UT when the Poincare Index changes its sign, indicating the existence of two opposite polarity nulls and a possible separator between them.

Figure 8 shows the original data (upper six plots) from Cluster satellites C1–C4 and the corresponding Poincare Index (the bottom plot), on 1 October 2001 between 09:47 UT and 09:50 UT in the GSE coordinate system. Clearly, the original data substantially fluctuate at the null position, with the Poincare Index jumping from ±1 to zero several times. Nevertheless, from the above investigations, we infer that such fluctuation does
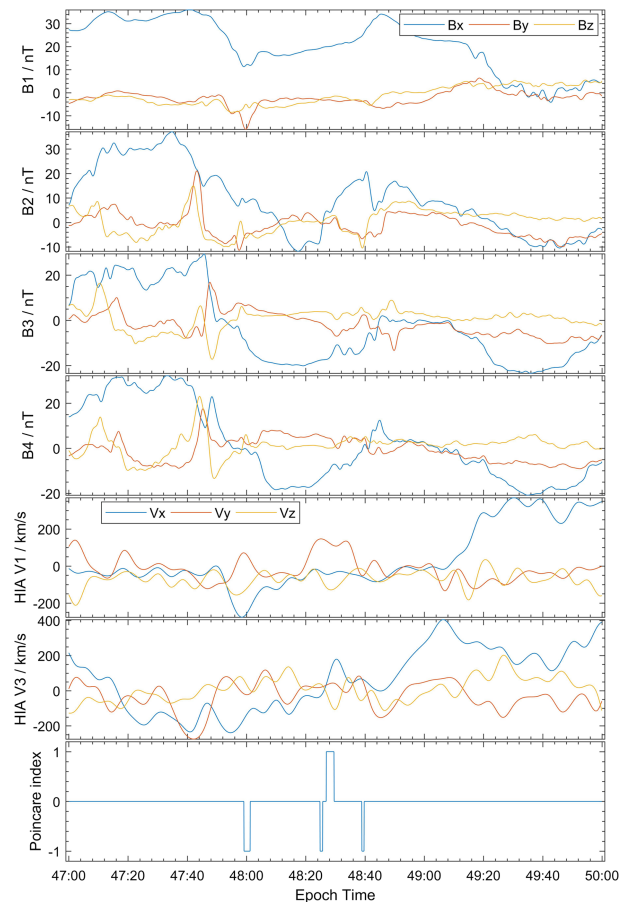

Figure 8. Data measured by Cluster satellites C1–C4 and corresponding Poincare Index on 1 October 2001 between 09:47 UT and 09:50 UT.
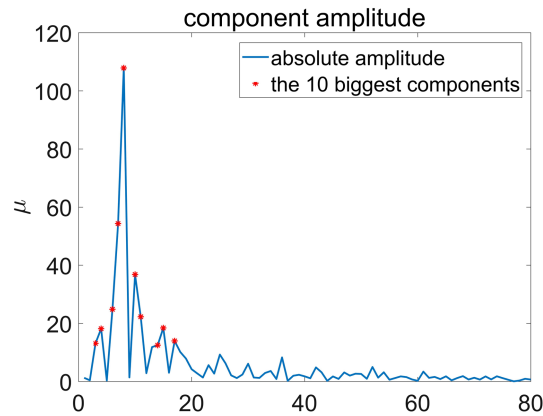
Figure 9. Component amplitudes of basic magnetic structures for Cluster data reconstruction.

not cause significant errors in the reconstruction results, indicating that we can use the original data for the reconstruction. However, we have to know the satellite positions relative to the magnetic structure or the magnetic structure velocity relative to the satellites. While DeHoffmann-Teller (HT) analysis (Khrabrov & Sonnerup, 1998) is best suited for the ideal MHD and the spatiotemporal difference (STD) method (Shi et al., 2006) assumes linear interpolation, both are inadequate due to nonideality and the short scale length indicating a diffusion region around the magnetic null. Thus, we here treat the velocity as a hyper-parameter to tune, demanding that the relative error, which is defined by the average error of $\left| \Delta \vec{B} \right| \equiv | \vec{B}_{\text{model}} - \vec{B}_{\text{rec}} |$ from all measurement positions, be as small as possible to keep the error-level low. Note that the structure moves tailward from the data of 47:00–49:00 UT because of both B_z and V_x changing sign from minus to plus. Then we assume the structure mainly moving in the minus x-direction in the GSE coordinates. And note that when C1 is clearly in the outer MHD region (with a significant $B_x \sim 20$–30 nT), the bulk velocity in the x-direction varies within a range of -200 to 0 km/s, the bulk velocity in the y-direction varies within a range of 0 to 150 km/s, and the bulk velocity in the z-direction varies within a range of -100 to 0 km/s. Thus, we search the optimal x-component of the velocity by setting the other two components to be zeros first, due to the x-direction motion being the main movement. Then, fixing the optimal x-component, we search the optimal y-component, due to its obviousness, by setting z-component to be zero. Finally, fixing the optimal y-component additionally, we search the optimal z-component. Each time we take 21 observations, thus 84 observed magnetic vectors, to form a 172-dimensional measurement value vector. At the same time, we place 40 nodes around the measurement region, in a way as shown in Figure 1. Thus, there are 80 unknown parameters forming an 80-dimensional expansion coefficient vector. Then we obtain 80 non-vanishing singular values, and therefore, 80 magnetic field value vectors whose amplitudes are like those shown in Figure 9.

We keep the largest 10 in the first 20 components to avoid violent fluctuation that may be caused by small singular values. The obtained relative errors are shown in Table 3, and the optimal velocity is $(-200, 100, 0)$ km/s. The obtained reconstructed field is shown in Figure 10. The maximum magnetic field intensity in the whole reconstructed region is around 50 nT which is on the order of the observed maximum of 30 nT, meaning there is no significant fluctuation in the reconstructed field. In addition, there is an A_s-type and a B-type nulls, consistent with the Poincare Index. The nulls are connected by a separator, and their

Table 3
Reconstructed Results From Different Velocities

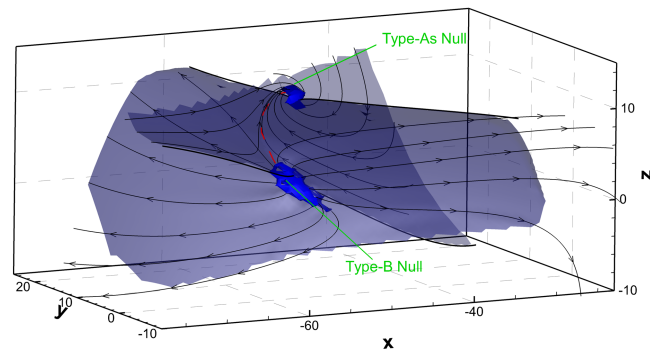| Velocity (km/s)	$(-100, 0, 0)$	$(-200, 0, 0)$	$(-300, 0, 0)$
Average error (nT)	3.55	3.04	3.27
Velocity (km/s)	$(-200, 50, 0)$	$(-200, 100, 0)$	$(-200, 150, 0)$
Average error (nT)	4.67	2.14	2.25
Velocity (km/s)	$(-200, 100, 50)$	$(-200, 100, 100)$	
Average error (nT)	2.33	2.84	—

Figure 10. The reconstructed field of 1 October 2001 reconnection event, with two nulls indicated by purple contours for magnitude of $\vec{B}$ being 0.8 nT. Black streamlines are magnetic lines, bold black lines are γ-lines, and the red line represents the separator. The shading surfaces are Σ surfaces of nulls. The unit of the coordinates is km.

separation is 1,478 km $\approx 1.12 d_i$, where $d_i = 1,320$ km is the ion inertial length for the ion density of 0.03 cm^{-3}. These results are also consistent with previous findings (Guo et al., 2013; Xiao et al., 2007) but without a priori imposed current system.

5. Conclusion

The reconstruction of complicated 3D global or local magnetic geometries is very important in space physics, since it helps to understand the correlated physical processes. High-resolution measurements of multi-spacecraft missions such as Cluster and particularly MMS make the task realistic. Here we develop a new method to reconstruct the complex geometry of local magnetic structures from a time series of spacecraft data, by expanding magnetic field into a set of modified radial basis functions (M-RBF) to relax the restrictions on magnetic structures. When expressing the reconstruction scheme in a matrix form, we apply the singular value decomposition to solve the rank deficient inversion problem, to find an optimal solution vector with the smallest norm. Numerically, we need to totally ignore those small singular values, to make the norm of solution vector α as small as possible to avoid large fluctuation and meanwhile keep the discrepancy between the measured and reconstructed field vectors as small as possible. We applied the method to several model magnetic geometries to test its ability to ensure a good agreement with preset model field, even with random errors added. Furthermore, we applied it to a Cluster observation event to justify our method. Without a priori imposed current sheet beforehand, we are still able to reconstruct the geometry of separator reconnection, consistent with previous studies. However, owing to the large separation of Cluster spacecraft, it is hard to accurately determine the structure's velocity. This could be remedied by using MMS data, where the spacecraft separation is commensurate with the electron skin depth scale. Thus, applying the method to MMS data may result in much more detailed and more accurate reconstructions.

References

Andreeva, V. A., & Tsyganenko, N. A. (2016). Reconstructing the magnetosphere from data suing radial basis functions. *Journal of Geophysical Research: Space Physics*, *121*, 2249–2263. https://doi.org/10.1002/2015JA022242

Birn, J., Drake, J. F., Shay, M. A., Rogers, B. N., Denton, R. E., Hesse, M., et al. (2001). Geospace environmental modeling (GEM) magnetic reconnection Challenge. *Journal of Geophysical Research*, *106*(A3), 3737–3750. https://doi.org/10.1029/1999JA001001

Eastwood, J. P., Phan, T.-D., Mozer, F. S., Shay, M. A., Fujimoto, M., Retinò, A., et al. (2007). Multi-point observations of the Hall electromagnetic field and secondary island formation during magnetic reconnection. *Journal of Geophysical Research*, *112*, A06235. https://doi.org/10.1029/2006JA012158

Golub, G. H. (1970). Singular value decomposition and least squares solutions. *Numerische Mathematik*, *14*(5), 403–420. https://doi.org/10.1007/BF02163027

Greene, J. M. (1992). Locating three-dimensional roots by a bisect ion method. *Journal of Computational Physics*, *98*, 193–198. https://doi.org/10.1016/0021-9991(92)90137-N

Guo, R. L., Pu, Z. Y., Xiao, C. J., Wang, X. G., Fu, S. Y., Xie, L., et al. (2013). Separator reconnection with antiparallel/component features observed in magnetotail plasmas. *Journal of Geophysical Research: Space Physics*, *118*, 6116–6126. https://doi.org/10.1002/jgra.50569

Hasegawa, H., Denton, R. E., Nakamura, R., Genestreti, K. J., Nakamura, T. K. M., Hwang, K.-J., et al. (2019). Reconstruction of the electron diffusion region of magnetotail reconnection seen by the MMS spacecraft on 11 July 2017. *Journal of Geophysical Research: Space Physics*, *124*, 122–138. https://doi.org/10.1029/2018JA026051

Hasegawa, H., Sonnerup, B. U. Ö., Eriksson, S., Nakamura, T. K. M., & Kawano, H. (2015). Dual-spacecraft reconstruction of a three-dimensional magnetic flux rope at the Earth's magnetopause. *Annales Geophysicae*, *33*(2), 169–184. https://doi.org/10.5194/angeo-33-169-2015

Hau, L.-N., & Sonnerup, B. U. Ö. (1999). Two-dimensional coherent structures in the magnetopause: Recovery of static equilibria from single-spacecraft data. *Journal of Geophysical Research*, *104*, 6899–6917. https://doi.org/10.1029/1999JA900002

He, J. S., Tu, C. Y., Tian, H., Xiao, C. J., Wang, X. G., Pu, Z. Y., et al. (2008). A magnetic null geometry reconstructed from Cluster spacecraft observations. *Journal of Geophysical Research*, *113*, A05205. https://doi.org/10.1029/2007JA012609

Hu, Q., & Sonnerup, B. U. Ö. (2001). Reconstruction of magnetic flux ropes in the solar wind. *Geophysical Research Letters*, *28*, 467–470. https://doi.org/10.1029/2000GL012232

Khrabrov, A. V., & Sonnerup, B. U. Ö. (1998). DeHoffmann-Teller Analysis. In G. Paschmann & P. W. Daly (Eds.), *Analysis methods for multi-spacecraft data* (Chap. 9, pp. 221–248). Noordwijk: ESA Publications Division.

Lau, Y.-T., & Finn, J. M. (1990). Three-dimensional kinematic reconnection in the presence of field nulls and closed field lines. *The Astrophysical Journal*, *350*, 672–691. https://doi.org/10.1086/168419

Øieroset, M., Phan, T. D., Fujimoto, M., Lin, R. P., & Lepping, R. P. (2001). In situ detection of collisionless reconnection in the Earth's magnetotail. *Nature*, 412–414. https://doi.org/10.1038/35086520

Parker, E. (1957). Sweet's mechanism for merging magnetic fields in conducting fluids. *Journal of Geophysical Research*, *62*, 509. https://doi.org/10.1029/JZ062i004p00509

Pontin, D. I. (2011). Three-dimensional magnetic reconnection regimes: A review. *Advances in Space Research*, *47*, 1508–1522. https://doi.org/10.1016/j.asr.2010.12.022

Priest, E. R., & Titov, V. S. (1996). Magnetic reconnection at three-dimensional null points. *Philosophical Transactions of the Royal Society London A*, *354*(1721), 2951–2992. https://doi.org/10.1098/rsta.1996.0136

Pritchett, P. L. (2004). Three-dimensional collisionless magnetic reconnection in the presence of a guide field. *Journal of Geophysical Research*, *109*, A01220. https://doi.org/10.1029/2003JA009999

Runov, A., Nakamura, R., Baumjohann, W., Treumann, R. A., Zhang, T. L., Volwerk, M., et al. (2003). Current sheet structure near magnetic X-line observed by Cluster. *Geophysical Research Letters*, *30*(11), 1579. https://doi.org/10.1029/2002GL016730

Shi, Q. Q., Chen, C., Dunlop, M. W., Pu, Z. Y., Zong, Q. G., Liu, Z. X., et al. (2006). Motion of observed structures calculated from multi-point magnetic field measurements: Application to Cluster. *Geophysical Research Letters*, *33*, L08109. https://doi.org/10.1029/2005GL025073

Stern, D. P. (1976). Representation of magnetic fields in space. *Reviews of Geophysics and Space Physics*, *14*(2), 200. https://doi.org/10.1029/RG014i002p00199

Tsyganenko, N. A. (1995). Modeling the Earth's magnetospheric magnetic field confined within a realistic magnetopause. *Journal of Geophysical Research*, *100*(A4), 5599–5612. https://doi.org/10.1029/94JA03193

Tsyganenko, N. A. (2014). Data-based modeling of the geomagnetosphere with an IMF-dependent magnetopause. *Journal of Geophysical Research: Space Physics*, *119*, 335–354. https://doi.org/10.1002/2013JA019346

Tsyganenko, N. A., & Andreeva, V. A. (2016). An empirical RBF model of the magnetosphere parameterized by interplanetary and ground-based drivers. *Journal of Geophysical Research: Space Physics*, *121*, 10,786–10,802. https://doi.org/10.1002/2016JA023217

Xiao, C. J., Wang, X. G., Pu, Z. Y., Ma, Z. W., Zhao, H., Zhou, G. P., et al. (2007). Satellite observations of separator-line geometry of three-dimensional magnetic reconnection. *Nature Physics*, *3*(9), 609–613. https://doi.org/10.1038/nphys650

Xiao, C. J., Wang, X. G., Pu, Z. Y., Zhao, H., Wang, J. X., Ma, Z. W., et al. (2006). In situ evidence for the structure of the magnetic null in a 3D reconnection event in the Earth's magnetotail. *Nature Physics*, *2*(7), 478–483. https://doi.org/10.1038/nphys342

Yamada, M., Kulsrud, R., & Ji, H. (2010). Magnetic reconnection. *Reviews of Modern Physics*, *82*(1), 603–664. https://doi.org/10.1103/RevModPhys.82.603